Statistical Analysis and Modeling of a Quadrotor's Radar Cross-Section

Tiago O. Costalonga [*,†], Willian S. L. Soares [‡], Vanessa P. R. Magri [*], Victor Fernandes [*]
Department of Telecommunications Engineering, Fluminense Federal University (UFF), Niterói-RJ, Brazil[*]
Navy's Acoustic and Electronic Warfare Center (CGAEM), Brazilian Navy, Niterói-RJ, Brazil[†]
Admiral Alexandrino Instruction Center (CIAA), Brazilian Navy, Rio de Janeiro-RJ, Brazil[‡]
Email: tiago_ogioni@id.uff.br,willian.sathler@marinha.mil.br,vanessamagri@id.uff.br,fernandesvictor@id.uff.br

***Abstract*—This paper focuses on the statistical analysis and modeling of the radar cross-section (RCS) of a DJI Phantom IV drone. The RCS datasets are generated by means of simulations performed at 9.41 GHz for distinct azimuth and elevation angles. Further, these datasets are fitted to usual probability distributions using three criteria, namely log-likelihood (LLK), Akaike information criterion (AIC), and Bayesian information criterion (BIC). Moreover, the impacts of RCS modeling on the radar detection range is analyzed. Based on numerical results, the Exponential distribution is shown to be the best fit for the RCS datasets. A good agreement is obtained between the Exponential's probability distribution function and the histogram of datasets. Finally, the use of this distribution for modeling RCS datasets achieves a maximum error of 3.8% when applied to the radar range equation.**

***Keywords*—radar cross-section, statistic, drone, likelihood, Akaike, Bayesian.**

I. Introduction

Nowadays, a considerable increase in the quantity and popularity of Remotely Piloted Aircrafts (RPAs) is being observed worldwide. On one hand, they can be used in a vast variety of useful applications, such as entertainment, commerce, and even in healthcare [1]. On the other hand, these kinds of drones can also be aimed at negative goals including terrorism and espionage, thus, affecting security and privacy [2]. It is necessary to come out with ways of countering the aforementioned threats caused by the widespread of RPAs.

In this regard, numerous works are focusing on radar detection of RPAs due to its advantages in relation to other methods of detection. One may highlight the efficiency in adverse weather conditions (i.e., fog, rain, or snow) and easily deploy on different platforms on land, sea, or air [3]. A radar system is responsible for emitting electromagnetic waves, and, then, analyzing echoes that reflect on the targets. Moreover, by analyzing some aspects of the echoes such as time of arrival, amplitude, and frequency shift, the radar system can estimate the distance, size, speed, and even the shape of the detected targets [4].

Radar Cross-Section (RCS) is a crucial parameter for radar detection, as it measures the reflectivity of targets and plays a pivotal role in determining the detectability of them by radar systems. It depends on factors, such as the size, shape, and composition of the target as well as the frequency of the incident electromagnetic wave [5]. Basically, targets with high RCS are more reflective and easier for radar systems to detect, while targets with low RCS are less reflective and harder to detect. Moreover, targets with a complex structure and geometry have a unique RCS signature that can be used for target identification [3].

For example, [6] investigated the influence of a small fixed-wing RPA's RCS on the detection range of an anti-drone system. Simulations of the drone's monostatic RCS were performed using real parameters of two radars, with operating frequencies of $8.70 - 9.65$ GHz and $3 - 16$ GHz. They found out that the RPA's mean RCS were -17.62 dBsm and -22.77 dBsm each, achieving a detection range of 1784 m. In [7], the authors measured and analyzed the monostatic RCS of nine different types of drones in an anechoic chamber, with frequencies varying from 26 GHz to 40 GHz. They showed that drones made of carbon fiber are easier to detect than the ones made from plastic and styrofoam. In [8], a drone classification was proposed by means of the monostatic RCS dataset provided by [7]. The classification through the drone's RCS signature was made by a new deep-learning technique, the so-called LSTM-ALRO. Accordingly, it was possible to achieve 99.88% of detection accuracy when compared with the existing drone classification model. Finally, [9] analyzed the RCS statistical properties of nine different commercial drones. To perform such analysis, they measured their monostatic RCS in an anechoic chamber at 9 GHz. According to them, the RCS behavior of investigated

979-8-3503-4357-1/23/$31.00

drones is rather in agreement with a random variable than a single constant number.

In general, previous works investigated the empirical values of RCS by solely measuring and analyzing them in deterministic terms. To the best of the authors' knowledge, the statistical analysis and modeling of RPAs' RCS have not been thoroughly explored in the literature. Thus, this work proposes a statistical approach for modeling the RCS of a commercial drone, DJI Phantom IV, employing a probability distribution that provides the best agreement with the histogram of a simulated RCS dataset. The RCS dataset was generated by simulations performed with Feko® software. The angles of azimuth and elevation of the incident wave were varied from $0°$ to $360°$ and from -$90°$ to $90°$, respectively. Finally, but not least, comparative analyses between the chosen probability distribution and the RCS dataset are provided, in addition to an evaluation of the radar detection range.

The remainder of this work is organized as follows: Section II introduces the mathematical formulation of RCS, criteria for selecting the probability distribution, and radar range. Section III presents the methodology to carry out statistical analysis and modeling. Section IV discusses numerical results, while Section V presents final remarks.

II. Mathematical Formulation

First, this section introduces the mathematical formulation of RCS and its defining characteristics. Then, it formulates the criteria used for statistical analysis of a RCS dataset. Lastly, it presents the radar range equation and its parameters.

A. Radar Cross-Section

The Institute of Electrical and Electronics Engineers (IEEE) defines RCS as a measure of power scattered in a given spatial direction when a target is illuminated by an electromagnetic plane wave [10]. The plane wave assumption is made when the distance between the radar and the target is fairly large. The region comprehended above this distance is called the far field, and it will be assumed for the RCS mathematical formulation. Thus, the RCS of the target is expressed as

$$\sigma = \lim_{R\to\infty} 4\pi R^2 \frac{|E_s|^2}{|E_i|^2}, \tag{1}$$

in which E_s (V/m) and E_i (V/m) are the far-field scattered and incident electric field intensities, respectively, at a distance R (m).

The mechanism of scattering depends on body size (L) relative to the wavelength (λ) of the incident wave. There are three scattering regions: Rayleigh, Resonant, and Optics. The Rayleigh region is defined for $L \ll \lambda$, where the scattering is induced by dipole moments, i.e., the incident electromagnetic wave interacts with the target and induces an electric current on its surface. The induced current then radiates a secondary electromagnetic wave, the scattered one. The resonant region occurs when $L \approx \lambda$, in which surface wave effects such as edge, traveling, and creeping waves along with optical effects are relevant. Finally, the Optics region is established when $L \gg \lambda$, resulting in insignificant surface wave effects whereas only optical effects take place [4]. In practical terms, these regions are limited by $L < \lambda$ (Rayleigh), $\lambda < L < 10\lambda$ (Resonant) and $L > 10\lambda$ (Optics). Figure 1 shows a sphere's RCS in these three regions, in which σ is normalized regarding the projected area of the sphere (i.e., the area of a circle, πa^2) and the sphere circumference is normalized by the wavelength (λ).

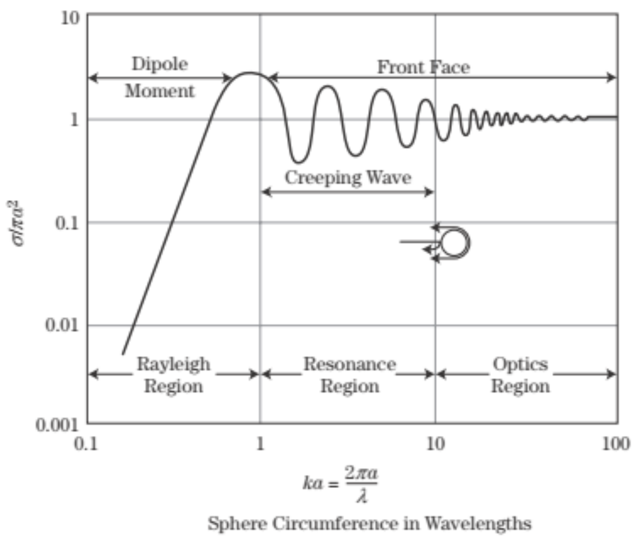

Figure 1: Normalized sphere's RCS in Rayleigh, Resonance, and Optics regions [11].

Unlike geometric targets such as spheres and corner reflectors, which have a deterministic value for the RCS, the RCS of real and complex targets may not be effectively modeled as a single constant [11]. For these targets, the RCS strongly varies with both azimuth and elevation angles, frequency, and polarization of the radar transmitter and receiver parts. As a consequence, the RCS must be estimated by fitting an RCS dataset's histogram to distinct probability distributions [3]. This statistical analysis leads to statistical models, which can be of utmost importance for precisely investigating the RCS impact on radar detection.

B. Statistical Analysis and Modeling

In this study, three statistical criteria will be used to perform probability distributions selection: Maximum

Likelihood Estimation (MLE), Akaike Information Criterion (AIC), and Bayesian Information Criterion (BIC).

MLE is a method of estimating the parameters ($\boldsymbol{\theta}$) of an assumed probability distribution, given some observed data ($\boldsymbol{X}$). This is achieved by maximizing a likelihood function so that, under the assumed probability distribution, the observed data is most probable. In other words, the parameters of each probability distribution are varied, and the one with the maximum likelihood score, in relation to the histogram generated with the samples of the simulated RCS, is selected [12]. Defining $\mathcal{S}_{rv} = \{pd_0, pd_1, \ldots, pd_{m-1}\}$ as the set of probability distributions, the likelihood of parameters $\boldsymbol{\theta} = \{\theta_0, \theta_1, \theta_2, \ldots, \theta_{k-1}\}$ of the j-th probability distribution in $\mathcal{S}_{rv}$, considering an independent and identically distributed random sample data set $\boldsymbol{X} = \{x_0, x_1, x_2, \ldots, x_{n-1}\}$, is given by

$$\mathcal{L}_j(\boldsymbol{\theta}) = \prod_{i=0}^{n-1} f(\boldsymbol{\theta}|x_i), \tag{2}$$

$\forall j \in \{0, 1, \ldots, m-1\}$, where $f(\boldsymbol{\theta}|x_i)$ is the likelihood of parameters $\boldsymbol{\theta}$ for a single outcome $x_i \in \boldsymbol{X}$.

In practice, it is often convenient to work with the natural logarithm of the likelihood function, called the log-likelihood (LLK), which can be expressed as

$$\mathrm{LLK}_j(\boldsymbol{\theta}) = \ln\{\mathcal{L}_j(\boldsymbol{\theta})\} = \sum_{i=1}^{n} \ln\{f(\boldsymbol{\theta}|x_i)\}. \tag{3}$$

Since the logarithm is a monotonic function, the maximum of $\mathrm{LLK}_j(\boldsymbol{\theta})$ occurs at the same value of $\boldsymbol{\theta}$ as does the maximum of $\mathcal{L}_j(\boldsymbol{\theta})$. Once $\mathrm{LLK}_j(\boldsymbol{\theta})$ is maximized, the parameters of the j-th probability distribution can be obtained through

$$\hat{\boldsymbol{\theta}}_{\mathrm{LLK}_j} = \arg\max_{\boldsymbol{\theta}} \mathrm{LLK}_j(\boldsymbol{\theta}). \tag{4}$$

MLE is a usual criterion to estimate the best probability distribution which fits the dataset. However, it does not consider the effect of overfitting the dataset. The fit of any model can be improved by increasing the number of parameters, but there is a trade-off in the increasing variance [12]. Overfitting can be taken into account by penalizing the complexity of the given probability distribution. AIC and BIC criteria take this in consideration for the j-th probability distribution in $\mathcal{S}_{rv}$, respectively, through

$$\mathrm{AIC}_j(\boldsymbol{\theta}) = -2\mathrm{LLK}_j(\boldsymbol{\theta}) + 2k \tag{5}$$

and

$$\mathrm{BIC}_j(\boldsymbol{\theta}) = -2\mathrm{LLK}_j(\boldsymbol{\theta}) + k \ln n, \tag{6}$$

$\forall j \in \{0, 1, \ldots, m-1\}$, in which k is the number of parameters of the j-th probability distribution and n is the number of samples of the dataset. As it can be seen, for AIC and BIC, the penalty terms are $2k$ and $k \ln n$, respectively. This means that AIC puts larger penalty on probability distribution functions with higher number of parameters, while BIC additionally penalizes the ones regarding the number of samples contained in the dataset. In general, the best probability distribution model is the one with either the lowest AIC or BIC score [3]. Thus, the j-th probability distribution parameters can be obtained by minimizing AIC and BIC scores, respectively, as

$$\hat{\boldsymbol{\theta}}_{\mathrm{AIC}_j} = \arg\min_{\boldsymbol{\theta}} \mathrm{AIC}_j(\boldsymbol{\theta}) \tag{7}$$

and

$$\hat{\boldsymbol{\theta}}_{\mathrm{BIC}_j} = \arg\min_{\boldsymbol{\theta}} \mathrm{BIC}_j(\boldsymbol{\theta}). \tag{8}$$

Since the actual score of the LLK, AIC and BIC criteria depend on the dataset sample values, it is often convenient to work with their normalized versions. This is achieved by means of

$$\overline{\mathrm{LLK}_j}(\hat{\boldsymbol{\theta}}_{\mathrm{LLK}_j}) = \frac{\mathrm{LLK}_j(\hat{\boldsymbol{\theta}}_{\mathrm{LLK}_j})}{\max\limits_{j} \mathrm{LLK}_j(\hat{\boldsymbol{\theta}}_{\mathrm{LLK}_j})}, \tag{9}$$

$$\overline{\mathrm{AIC}_j}(\hat{\boldsymbol{\theta}}_{\mathrm{AIC}_j}) = \frac{\mathrm{AIC}_j(\hat{\boldsymbol{\theta}}_{\mathrm{AIC}_j})}{\max\limits_{j} \mathrm{AIC}_j(\hat{\boldsymbol{\theta}}_{\mathrm{AIC}_j})}, \tag{10}$$

and

$$\overline{\mathrm{BIC}_j}(\hat{\boldsymbol{\theta}}_{\mathrm{BIC}_j}) = \frac{\mathrm{BIC}_j(\hat{\boldsymbol{\theta}}_{\mathrm{BIC}_j})}{\max\limits_{j} \mathrm{BIC}_j(\hat{\boldsymbol{\theta}}_{\mathrm{BIC}_j})}, \tag{11}$$

respectively. In the manner that it is obtained $\overline{\mathrm{LLK}_j}(\hat{\boldsymbol{\theta}}_{\mathrm{LLK}_j}) \in [0, 1], \overline{\mathrm{AIC}_j}(\hat{\boldsymbol{\theta}}_{\mathrm{AIC}_j}) \in [-1, 0]$, and $\overline{\mathrm{BIC}_j}(\hat{\boldsymbol{\theta}}_{\mathrm{BIC}_j}) \in [-1, 0]$. For simplicity, (9), (10), (11) will be denoted, respectively, by $\overline{\mathrm{LLK}_j}$, $\overline{\mathrm{AIC}_j}$, and $\overline{\mathrm{BIC}_j}$ from now on. In this manner, the best probability distribution, for each criterion and for each $\boldsymbol{\alpha_i}$, is the one with the best score, i.e., $\overline{\mathrm{LLK}_j} = 1$ or $\overline{\mathrm{AIC}_j} = -1$ or $\overline{\mathrm{BIC}_j} = -1$.

C. Radar Range Equation

According to [4], the maximum detection range achieved by a radar system is given by

$$R_{\max}^4 = \frac{P_t G^2 \lambda^2 \sigma}{(4\pi)^3 NF k T_0 B L_s L_f \mathrm{SNR}}, \tag{12}$$

in which P_t is the peak transmit power (W), G are the transmitter and receiver antenna gain, λ is the wavelength (m) of the electromagnetic wave, σ is the RCS of the target (m^2), NF is the receiver noise figure of the radar, k is the Boltzmann constant ($1,38.10^{-23}$ J/K), T_0 is the temperature (K), B is the receiver bandwidth (Hz), L_s is the system loss, L_f is the target fluctuation loss, and SNR is the signal-to-noise ratio minimum necessary to detect a target with an RCS equal σ. Note that, except for L_f and σ, all other parameters depend uniquely on the radar design characteristics.

III. Methodology

The quadrotor investigated in this work is the DJI Phantom IV, shown in Figure 2. This drone has a body size (L) of approximately 35 cm diagonally, and it weighs around 1.38 kg. It basically consists of a main body, four propellers, and a high-resolution camera. Most of its structure is built of plastic.

Figure 2: DJI Phantom IV drone.

To create the RCS's dataset, it was used Feko® software from Altair® company. To do so, the simulations were performed by assuming a horizontally polarized plane wave at 9.41 GHz (i.e., $\lambda = 0.0319$ m). Moreover, the plane wave incidence occurred in the far-field region on the three-dimensional model of the drone, as illustrated in Figure 3. The assumed azimuth and elevation angles of the incident wave are, respectively, $\boldsymbol{\phi} = \{\phi_0, \phi_1, \ldots, \phi_{N_a-1}\}$ and $\boldsymbol{\alpha} = \{\alpha_0, \alpha_1, \ldots, \alpha_{N_e-1}\}$, where N_a and N_e represents the size of $\boldsymbol{\phi}$ and $\boldsymbol{\alpha}$, respectively. The RCS dataset is given by $\boldsymbol{\sigma} = \{\sigma_0, \sigma_1, \ldots, \sigma_{N_a-1}\}$, in which each element of it corresponds to the simulated RCS value of a single azimuth angle for a fixed elevation angle (i.e., an $\boldsymbol{\alpha}$ element). The method used to simulate the samples of the drone's RCS was Physical Optics because $L > 10\lambda$ characterizes the Optics scattering region.

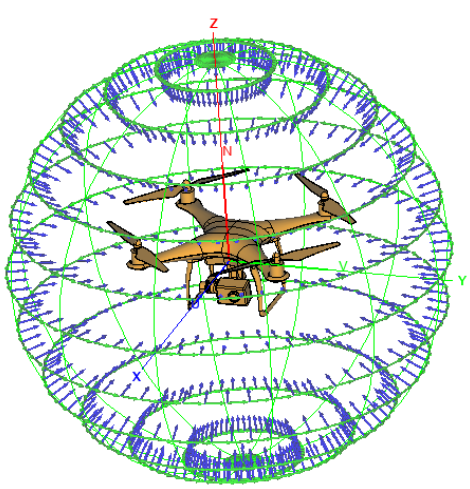

Figure 3: RCS simulation of DJI Phantom IV in Feko®.

The set of probability distributions, $\mathcal{S}_{rv} = \{$*Exponential, Gamma, Generalized Extreme Value, Generalized Pareto, Rician, Log-normal, Nakagami, Rayleigh, Weibull*$\}$, were chosen to model random variables belonging to $\mathbb{R}_+$ and that are commonly used in the telecommunications field. In this regard, the statistical modeling is realized as follows:

- **Step 1**: Select α_i, defining a unique RCS dataset $\boldsymbol{\sigma}$ for modeling with a fixed elevation angle.
- **Step 2**: For each S_{rv} element, calculate $\overline{\text{LLK}_j}$, $\overline{\text{AIC}_j}$, and $\overline{\text{BIC}_j}$ scores by means of (9), (10) and (11), respectively.
- **Step 3**: Evaluate the number of occurrences of i) $\overline{\text{LLK}_j} = 1$, ii) $\overline{\text{AIC}_j} = -1$, and iii) $\overline{\text{BIC}_j} = -1$. These are denoted $N_{\text{LLK}_j}, N_{\text{AIC}_j}$, and N_{BIC_j}, respectively, for the j-th probability distribution. They are incremented for each α_i.
- **Step 4**: Return to Step 1 for another not previously selected α_i, until there is unused $i \in \{0, 1, \ldots, N_e - 1\}$. This step occurs N_e times.
- **Step 5**: Calculate the relative frequencies $R_{\text{LLK}_j} = N_{\text{LLK}_j}/N_e$, $R_{\text{AIC}_j} = N_{\text{AIC}_j}/N_e$, and $R_{\text{BIC}_j} = N_{\text{BIC}_j}/N_e$.
- **Step 6**: Evaluate the average relative frequencies $R_{avg_j} = (R_{\text{LLK}_j} + R_{\text{AIC}_j} + R_{\text{BIC}_j})/3$.
- **Step 7**: The chosen probability distribution to model the datasets for every element of $\boldsymbol{\alpha}$ is the one with the highest $R_{avg_j}, \forall j \in \{0, 1, \ldots, m-1\}$ associated with the set $\mathcal{S}_{rv}$.

IV. Numerical Results

The RCS simulation assumed $\boldsymbol{\phi} = \{0°, 2°, \ldots, 360°\}$ and $\boldsymbol{\alpha} = \{-90°, -85°, \ldots, 90°\}$. In order to analyze the impacts of RCS modeling in (12), specifications of a usual maritime radar were considered. The radar model is FAR-2117 from Furuno® company and its specifications are horizontal-polarized antenna with $G = 31.5$ dB, operational frequency $f = 9.41$ GHz, $P_t = 12$ kW, $B = 60$ MHz, $NF = 6$ dB, and $L_s = 6$ dB [13].

Table I shows the normalized scores that each probability distribution achieved, for $\boldsymbol{\alpha}$ varying in steps of $10°$ for better presentation. The colored cells represent the best probability distribution for each criterion, being the yellow ones for $\overline{\text{LLK}_j}$, green ones for $\overline{\text{AIC}_j}$ and blue ones for $\overline{\text{BIC}_j}$. For Table I and Figure 4, the probability distributions are numbered as follows: 1-Exponential, 2-Gamma, 3-Generalized Extreme Value, 4-Generalized Pareto, 5-Rician, 6-Log-normal, 7-Nakagami, 8-Rayleigh and 9-Weibull.

Note that, for LLK, the best fitting is the Generalized Pareto probability distribution. However, when introduced the penalizing factor for the number of parameters in AIC and BIC, the Generalized Pareto function

Table I: $\overline{\text{LLK}_j}$, $\overline{\text{AIC}_j}$ and $\overline{\text{BIC}_j}$ scores for each probability distribution at some elevation angles.

Probability Distributions		Elevation Angle (α) -90°	-80°	-70°	-60°	-50°	-40°	-30°	-20°	-10°	0°	10°	20°	30°	40°	50°	60°	70°	80°	90°
1	$\overline{\text{LLK}_1}$	-0.244	0.921	0.999	0.967	0.990	0.983	0.965	0.982	0.999	0.998	0.999	0.999	0.991	0.982	0.997	0.994	0.994	0.989	-0.595
	$\overline{\text{AIC}_1}$	0.246	-0.931	-1	-0.969	-0.992	-0.985	-0.968	-0.984	-1	-1	-1	-1	-0.992	-0.986	-1	-0.999	-1	-0.996	0.602
	$\overline{\text{BIC}_1}$	0.249	-0.939	-1	-0.973	-0.995	-0.988	-0.971	-0.986	-1	-1	-1	-1	-0.995	-0.989	-1	-1	-1	-1	0.614
2	$\overline{\text{LLK}_2}$	0.984	0.973	1	0.999	1	0.998	0.997	0.997	0.999	0.998	1	0.999	1	0.988	0.997	0.994	0.995	0.999	0.965
	$\overline{\text{AIC}_2}$	-0.985	-0.978	-0.997	-0.999	-1	-0.998	-0.999	-0.997	-0.998	-0.998	-0.998	-0.998	-1	-0.990	-0.997	-0.997	-0.996	-1	-0.967
	$\overline{\text{BIC}_2}$	-0.987	-0.978	-0.992	-0.999	-1	-0.998	-1	-0.996	-0.995	-0.994	-0.996	-0.995	-1	-0.990	-0.994	-0.993	-0.990	-0.993	-0.971
3	$\overline{\text{LLK}_3}$	1	0.956	0.962	0.981	0.991	0.980	1	0.980	0.981	0.970	0.975	0.984	0.993	0.965	0.956	0.992	0.983	0.922	1
	$\overline{\text{AIC}_3}$	-1	-0.955	-0.956	-0.978	-0.989	-0.978	-1	-0.978	-0.978	-0.967	-0.973	-0.981	-0.991	-0.965	-0.953	-0.992	-0.981	-0.915	-1
	$\overline{\text{BIC}_3}$	-1	-0.944	-0.947	-0.974	-0.985	-0.975	-0.998	-0.975	-0.972	-0.960	-0.967	-0.976	-0.989	-0.963	-0.946	-0.984	-0.969	-0.897	-1
4	$\overline{\text{LLK}_4}$	0.684	1	0.999	0.986	0.993	0.999	0.977	0.999	1	1	0.999	1	0.994	1	1	1	1	1	0.447
	$\overline{\text{AIC}_4}$	-0.683	-0.999	-0.994	-0.983	-0.991	-0.998	-0.977	-0.997	-0.996	-0.997	-0.997	-0.997	-0.992	-1	-0.997	-1	-0.997	-0.994	-0.442
	$\overline{\text{BIC}_4}$	-0.681	-0.990	-0.985	-0.979	-0.987	-0.995	-0.975	-0.994	-0.990	-0.990	-0.991	-0.991	-0.990	-0.997	-0.990	-0.992	-0.985	-0.977	-0.435
5	$\overline{\text{LLK}}$	0.984	0.838	0.703	0.938	0.879	0.943	0.970	0.621	0.807	0.823	0.834	0.815	0.922	0.917	0.789	0.634	0.509	0.580	0.965
	$\overline{\text{AIC}}$	-0.985	-0.841	-0.699	-0.938	-0.879	-0.943	-0.971	-0.620	-0.805	-0.822	-0.832	-0.814	-0.921	-0.919	-0.788	-0.634	-0.506	-0.575	-0.967
	$\overline{\text{BIC}}$	-0.987	-0.838	-0.693	-0.937	-0.878	-0.943	-0.972	-0.618	-0.802	-0.818	-0.829	-0.810	-0.921	-0.919	-0.784	-0.628	-0.497	-0.563	-0.971
6	$\overline{\text{LLK}}$	0.984	0.782	0.955	0.975	0.984	0.980	0.969	0.985	0.987	0.944	0.953	0.987	0.979	0.950	0.975	0.946	0.980	0.945	0.964
	$\overline{\text{AIC}}$	-0.985	-0.784	-0.952	-0.975	-0.984	-0.980	-0.971	-0.985	-0.986	-0.943	-0.952	-0.986	-0.979	-0.951	-0.974	-0.949	-0.981	-0.945	-0.967
	$\overline{\text{BIC}}$	-0.987	-0.780	-0.947	-0.974	-0.984	-0.980	-0.971	-0.985	-0.983	-0.940	-0.949	-0.983	-0.979	-0.951	-0.971	-0.945	-0.975	-0.938	-0.971
7	$\overline{\text{LLK}_7}$	0.984	0.994	0.984	0.995	0.985	0.999	0.991	0.979	0.988	0.997	0.999	0.984	0.991	0.997	0.997	0.958	0.958	0.982	0.965
	$\overline{\text{AIC}_7}$	-0.985	-1	-0.981	-0.995	-0.985	-0.999	-0.993	-0.979	-0.987	-0.997	-0.997	-0.982	-0.991	-0.999	-0.997	-0.960	-0.959	-0.982	-0.967
	$\overline{\text{BIC}_7}$	-0.987	-1	-0.976	-0.995	-0.985	-0.999	-0.994	-0.978	-0.984	-0.993	-0.995	-0.980	-0.991	-1	-0.994	-0.956	-0.952	-0.975	-0.971
8	$\overline{\text{LLK}}$	-0.105	0.838	0.703	0.938	0.879	0.943	0.970	0.621	0.807	0.823	0.834	0.815	0.922	0.917	0.789	0.634	0.509	0.580	-0.270
	$\overline{\text{AIC}}$	0.107	-0.847	-0.702	-0.940	-0.881	-0.945	-0.973	-0.622	-0.807	-0.824	-0.834	-0.815	-0.923	-0.921	-0.790	-0.636	-0.509	-0.581	0.275
	$\overline{\text{BIC}}$	0.109	-0.854	-0.701	-0.944	-0.883	-0.947	-0.976	-0.622	-0.806	-0.824	-0.833	-0.815	-0.925	-0.924	-0.789	-0.635	-0.507	-0.579	0.283
9	$\overline{\text{LLK}_9}$	0.981	0.987	0.999	1	0.998	1	0.996	1	0.999	0.999	0.999	0.999	0.999	0.991	0.997	0.995	0.997	0.998	0.958
	$\overline{\text{AIC}_9}$	-0.982	-0.993	-0.997	-1	-0.998	-1	-0.998	-1	-0.998	-0.998	-0.998	-0.998	-0.999	-0.993	-0.997	-0.998	-0.998	-0.999	-0.960
	$\overline{\text{BIC}_9}$	-0.983	-0.992	-0.992	-1	-0.998	-1	-0.998	-1	-0.995	-0.995	-0.995	-0.995	-0.999	-0.993	-0.994	-0.994	-0.99	-0.992	-0.964

presents a worst fitting than the Exponential probability distribution in both criteria. This occurs due to the lower number of parameters of the latter distribution. Figure 4 shows the relative frequency of all probability distributions for each criterion. Observe that, for the Generalized Pareto distribution, $R_{\text{LLK}_j} = 0.43$, $R_{\text{AIC}_j} = 0.16$, and $R_{\text{BIC}_j} = 0.08$, which gives $R_{avg_j} = 0.22$. On the other hand, the Exponential distribution has $R_{\text{LLK}_j} = 0$, $R_{\text{AIC}_j} = 0.35$, and $R_{\text{BIC}_j} = 0.46$, and thus $R_{avg_j} = 0.27$.

Once its average relative frequency was the greatest, the Exponential probability distribution is chosen to model the entire RCS datasets for all elevation angles individually. However, it is important to highlight that some elevation angles of the incident wave are not practical. Although the RCS has been simulated for $\boldsymbol{\alpha}$ varying from -90° up to 90°, typical maritime radars have 30° of beam width vertical aperture, corresponding to $\boldsymbol{\alpha}$ being bounded between -15° and 15°. Table II shows γ values for all simulated elevation angles.

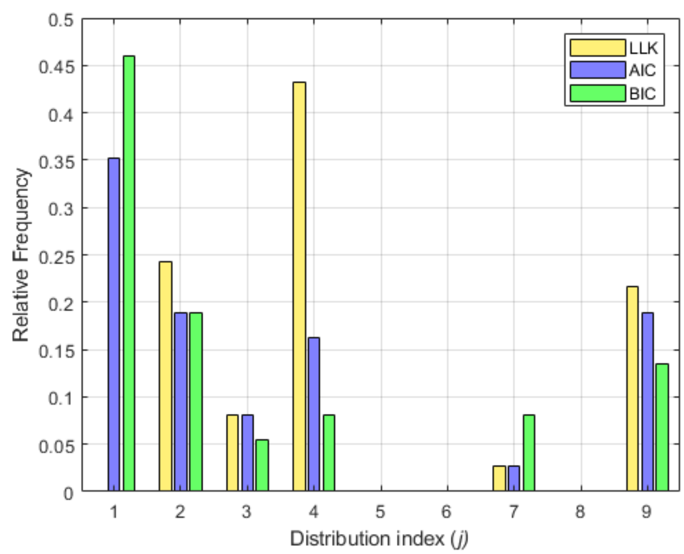

Figure 4: Relative frequency of each probability distributions for LLK, AIC, and BIC.

To perform the analysis of the PDF and CDF of the exponential probability distribution, it is used the horizontal plane of the radar antenna corresponding to an elevation angle $\alpha_i = 0°$. Consider σ_{pd} the RCS values for the Exponential distribution and σ_{ds} the simulated RCS values for the dataset distribution, with $\sigma_{ds} \in \boldsymbol{\sigma}$ for $\alpha_i = 0°$. The Exponential's PDF, in function of σ_{pd}, is given by the following equation

$$f(\sigma_{pd}) = \begin{cases} \gamma e^{-\gamma \sigma_{pd}} & , \sigma_{pd} \geq 0 \\ 0 & , \sigma_{pd} < 0 \end{cases} \tag{13}$$

in which, $\gamma = 0.0284$ for $\alpha_i = 0°$. Figure 5 shows both the Exponential's PDF and the RCS dataset histogram for $\alpha_i = 0°$. Note that the RCS values, in the histogram,

Table II: Exponential's parameter γ for distinct elevation angles.

Elevation Angle (α)	**Exponential's Parameter** (γ)
-90º	1.2473
-85º	0.3144
-80º	0.1511
-75º	0.1210
-70º	0.0527
-65º	0.0457
-60º	0.0423
-55º	0.0292
-50º	0.0246
-45º	0.0206
-40º	0.0177
-35º	0.0121
-30º	0.0116
-25º	0.0162
-20º	0.0155
-15º	0.0235
-10º	0.0160
-5º	0.0236
0º	0.0284
5º	0.0119
10º	0.0112
15º	0.0122
20º	0.0123
25º	0.0125
30º	0.0099
35º	0.0176
40º	0.0175
45º	0.0205
50º	0.0310
55º	0.0405
60º	0.0405
65º	0.0535
70º	0.0835
75º	0.1056
80º	0.1502
85º	0.6645
90º	1.3116

have a higher density for $\sigma_{ds} \leq 0.01\ m^2$. Yet, from $0\ m^2$ to $0.03\ m^2$, density decreases from 30 to 15, which corresponds to, approximately, 50% drop. Moreover, the higher σ_{ds}, the lower the density, corresponding to a typical Exponential's PDF characteristic.

The Exponential's CDF, also in function of σ_{pd}, is given by the following equation

$$F(\sigma_{pd}) = \begin{cases} 1 - e^{-\gamma\sigma_{pd}} & ,\sigma_{pd} \geq 0 \\ 0 & ,\sigma_{pd} < 0 \end{cases} \tag{14}$$

in which, $\gamma = 0.0284$ for $\alpha_i = 0°$. Figure 6 shows the curves of both Exponential and dataset CDFs, $F_{ds}(\sigma_{ds})$. Note that, for a probability of 0.9, $\sigma_{pd} = 0.0655$ and $\sigma_{ds} = 0.0652$, which yields an error of $100 \times |\sigma_{pd} - \sigma_{ds}|/\sigma_{ds} = 100 \times |0.0655 - 0.0652|/0.0652 = 0.46\%$ between the RCS values. For a probability of 0.5, it is had $\sigma_{ds} = 0.0198\ m^2$ and $\sigma_{pd} = 0.0199\ m^2$, resulting in an error of 0.5%. Yet, for $\sigma_{pd} = \sigma_{ds} = 0.1m^2$, it can be seen that the Exponential's and dataset's CDFs

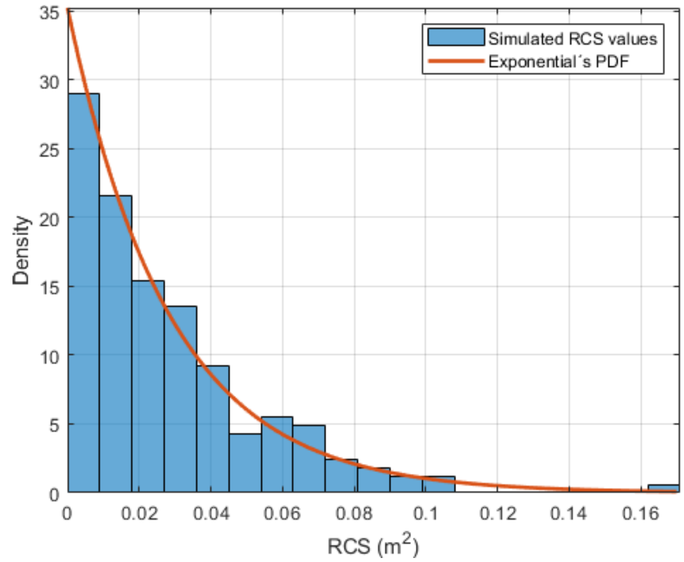

Figure 5: Histogram of simulated RCS values and PDF of the fitted Exponential distribution, when $\alpha_i = 0°$.

yields 0.97 and 0.99 of probability, respectively, which corresponds to 2% of difference.

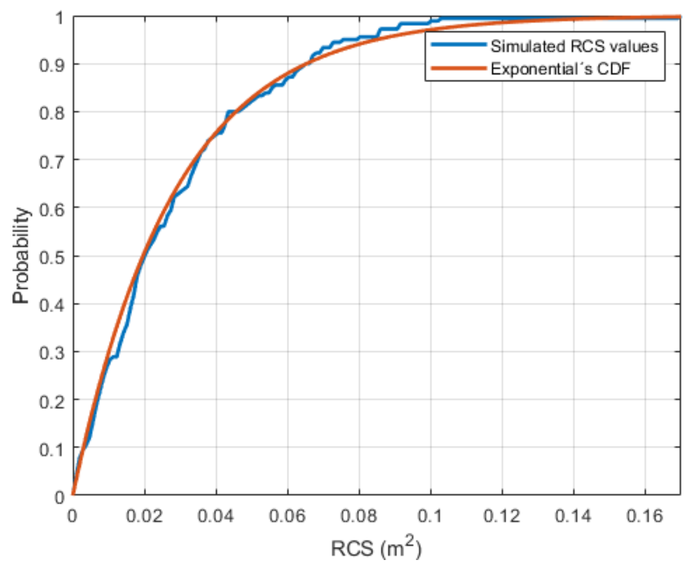

Figure 6: CDFs of the simulated RCS values and the fitted Exponential distribution, when $\alpha_i = 0°$.

To evaluate the impact of RCS modeling on (12), Figure 7 shows R_{max} as a function of SNR. These curves assume RCS values that satisfy $F(\sigma_{pd}) = F_{ds}(\sigma_{ds}) = 0.1, 0.3, \ldots, 0.9$. Observe that, for σ_{pd} and σ_{ds} that satisfies $F(\sigma_{pd}) = F_{ds}(\sigma_{ds}) = 0.1$, 0.5, and 0.9 the curves are well-fitted, presenting error less than 0.15%. The curve with the greatest error, about 3.8%, occurs for RCS values respecting $F(\sigma_{pd}) = F_{ds}(\sigma_{ds}) = 0.3$. Note that increasing both $F(\sigma_{pd})$ and $F_{ds}(\sigma_{ds})$ corresponds to an increment in the SNR for the same R_{max}.

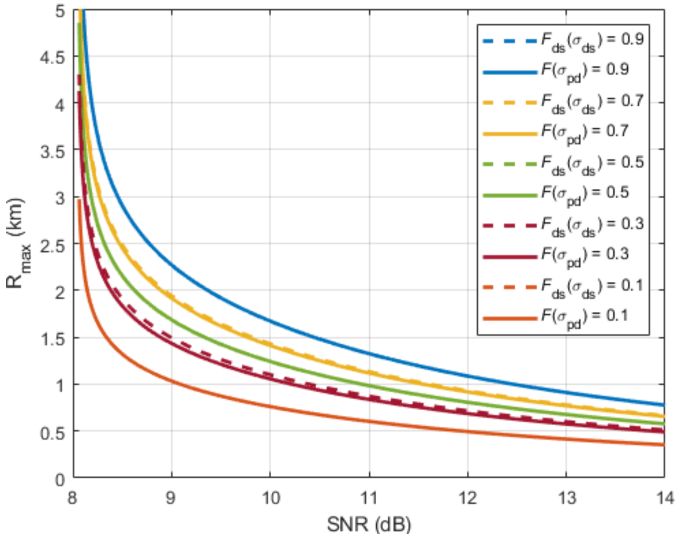

Figure 7: R_{max} as a function of SNR for some simulated RCS values.

V. Conclusions and Future Work

This paper discussed the statistical analysis and modeling of the DJI Phantom IV RCS for distinct elevation angles. For this, three different criteria to select the probability distribution which best fitted the RCS datasets were used. Simulations of RCS, analysis of the criteria LLK, AIC, BIC for various probability distributions, and calculation of radar range considering RCS as a random variable were carried out for this type of drone. Based on numerical results, the RCS dataset has been modeled as an Exponential probability distribution because it achieved the best averaged score in the used criteria. Considering the parameters of a maritime radar, it was shown that a maximum error of 3.8% in the radar range equation occurred. Further studies will be carried out to model the RCS as a random process for distinct frequencies, as well as for other types of drones.

Acknowledgement

This work was partially supported by the Brazilian Navy and the Brazilian Research Council CAPES by means of PROAP. Special thanks to Artur Martini Coelho Brandão, from AMB Serviços Eletrônicos company, for providing and maintaining the Furuno FAR-2117 radar.

References

[1] A. T. Sage *et al.*, “Testing the delivery of human organ transportation with drones in the real world,” *Science Robotics*, vol. 7, no. 73, p. eadf5798, 2022.

[2] J.-P. Yaacoub *et al.*, “Security analysis of drones systems: Attacks, limitations, and recommendations,” *Internet of Things*, vol. 11, p. 100218, 2020.

[3] M. Ezuma *et al.*, “Radar cross section based statistical recognition of uavs at microwave frequencies,” *IEEE Transactions on Aerospace and Electronic Systems*, vol. 58, no. 1, pp. 27–46, 2022.

[4] M. Skolnik, *Radar Handbook*, 3rd ed. New York: McGraw-Hill, 2008.

[5] E. F. Knott, J. F. Schaeffer, and M. T. Tulley, *Radar cross-section*, 2nd ed. SciTech Publishing, 2004.

[6] I. K. Kapoulas *et al.*, “Small fixed-wing UAV radar cross-section signature investigation and detection and classification of distance estimation using realistic parameters of a commercial anti-drone system,” *Drones*, vol. 7, no. 1, p. 39, 2023.

[7] V. Semkin *et al.*, “Analyzing radar cross section signatures of diverse drone models at mmwave frequencies,” *IEEE access*, vol. 8, pp. 48 958–48 969, 2020.

[8] R. Fu *et al.*, “Deep learning-based drone classification using radar cross section signatures at mmwave frequencies,” *IEEE Access*, vol. 9, pp. 161 431–161 444, 2021.

[9] P. Sedivy and O. Nemec, “Drone rcs statistical behaviour,” in *Proceedings of the MSG-SET-183 Specialists’ Meeting*, 2021, pp. 4–1–4–18.

[10] “IEEE standard dictionary of electrical and electronics terms,” *IEEE Transactions on Power Apparatus and Systems*, vol. PAS-99, no. 6, pp. 37a–37a, 1980.

[11] M. A. Richards *et al.*, *Principles of modern radar*, D. R. Kay, Ed. SciTech Publishing, 2010, vol. 1.

[12] K. P. Burnham and D. R. Anderson, *Model selection and multimodel inference: a practical information-theoretic approach*, 2nd ed. Springer-Verlag, 2004.

[13] T. O. Costalonga, V. P. R. Magri, and V. Fernandes, “Detecção de drone quadrotor por radar pulsado de banda X,” in *XLI Simp. Brasileiro de Telecom. e Processamento de Sinais*, 2023.